## **ORIGINAL PAPER**



# Multiscale computational modeling of aortic valve calcification

Javid Azimi-Boulali<sup>1</sup> · Gretchen J. Mahler<sup>2</sup> · Bruce T. Murray<sup>1</sup> · Peter Huang<sup>1</sup>

Received: 23 June 2023 / Accepted: 13 November 2023 © The Author(s), under exclusive licence to Springer-Verlag GmbH Germany, part of Springer Nature 2023

#### **Abstract**

Calcific aortic valve disease (CAVD) is a common cardiovascular disease that affects millions of people worldwide. The disease is characterized by the formation of calcium nodules on the aortic valve leaflets, which can lead to stenosis and heart failure if left untreated. The pathogenesis of CAVD is still not well understood, but involves several signaling pathways, including the transforming growth factor beta ( $TGF\beta$ ) pathway. In this study, we developed a multiscale computational model for  $TGF\beta$ -stimulated CAVD. The model framework comprises cellular behavior dynamics, subcellular signaling pathways, and tissue-level diffusion fields of pertinent chemical species, where information is shared among different scales. Processes such as endothelial to mesenchymal transition (EndMT), fibrosis, and calcification are incorporated. The results indicate that the majority of myofibroblasts and osteoblast-like cells ultimately die due to lack of nutrients as they become trapped in areas with higher levels of fibrosis or calcification, and they subsequently act as sources for calcium nodules, which contribute to a polydispersed nodule size distribution. Additionally, fibrosis and calcification processes occur more frequently in regions closer to the endothelial layer where the cell activity is higher. Our results provide insights into the mechanisms of CAVD and TGF $\beta$  signaling and could aid in the development of novel therapeutic approaches for CAVD and other related diseases such as cancer. More broadly, this type of modeling framework can pave the way for unraveling the complexity of biological systems by incorporating several signaling pathways in subcellular models to simulate tissue remodeling in diseases involving cellular mechanobiology.

 $\textbf{Keywords} \ \ CAVD \cdot Multiscale \ modeling \cdot EndMT \cdot Systems \ biology \cdot Calcification \cdot A ortic \ valve$ 

# 1 Introduction

Calcific aortic valve disease (CAVD) is the most predominant type of heart valve disease (Nkomo et al. 2006). CAVD is particularly widespread among the elderly in developed countries, and its healthcare burden is expected to increase with the global aging population (Yutzey et al. 2014). By

Peter Huang phuang@binghamton.eduJavid Azimi-Boulali

jazimib1@binghamton.edu

Gretchen J. Mahler gmahler@binghamton.edu

Bruce T. Murray bmurray@binghamton.edu

Published online: 13 December 2023

- Department of Mechanical Engineering, Binghamton University, Binghamton, NY 13902, USA
- Department of Biomedical Engineering, Binghamton University, Binghamton, NY 13902, USA

2050, the number of patients aged 75 and older with moderate to severe calcific aortic stenosis in the USA is projected to more than double (Benjamin et al. 2019). CAVD is a chronic disease that progresses from nanoscale calcific nodule formation to micro- and macro-scale nodules, resulting in severe stenosis due to progressive fibrotic tissue remodeling and mineralization (Fig. 1a) (Mathieu et al. 2015). Unfortunately, no treatment currently exists for valvular calcification, and patients typically do not experience symptoms until the disease has progressed significantly. At an advanced stage, valvular replacements are necessary to restore healthy physiology. Moreover, flow disturbances resulting from calcified valves can have downstream effects on the vascular system, as the aortic valve regulates blood flow into the vascular system (Misfeld and Sievers 2007) (Tables 1, 2).

Current research indicates that valvular disease is an active procalcific process that results in severe extracellular matrix (ECM) remodeling, fibrosis, and calcification (Rajamannan et al. 2011; Leopold 2012; Aikawa and Libby 2017).



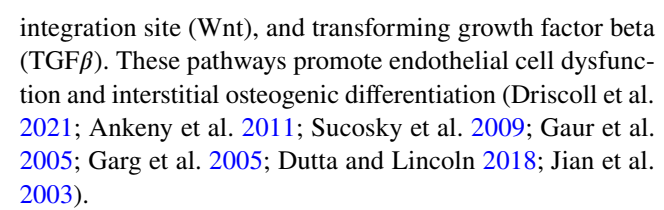
Table 1 List of nonstandard abbreviations and acronyms

Abbreviation	Definition
CAVD	Calcific aortic valve disease
ECM	Extracellular matrix
CPM	Cellular Potts model
$TGF\beta$	Transforming growth factor beta
MMP-9	Matrix metallopeptidase 9
$\alpha$ SMA	Alpha smooth muscle actin
LDL	Low-density lipoprotein
MCS	Monte Carlo step
PECAM-1	Platelet endothelial cell adhesion molecule 1
GAG	Glycosaminoglycan
BMP	Bone morphogenic protein
Wnt	Wingless-related integration site
VEC	Valvular endothelial cell
VIC	Valvular interstitial cell

Table 2 List of mathematical symbols used in the paper

Symbol	Meaning	
σ	Model cell	
τ	Model cell type	
J	Contact energy per unit area	
$\delta_{ij}$	Kronecker delta	
$H_c$	Contact energy	
$H_{cst}$	Constraint energy	
$H_{v}$	Volume constraint energy	
$H_m$	Motility energy	
$H_f$	Force energy	
$H_{ch}$	Chemotaxis energy	
$\lambda_{v}$	Volume constraint intensity	
$\lambda_{ch}$	Chemotaxis intensity	
$\lambda_f$	Force intensity	
v	Model cell volume	
$v_t$	Model cell target volume	
$T_m$	Pseudo-temperature in CPM	
D	Diffusion coefficient	
k	Chemical decay rate	
S	Secretion rate	
$C_n$	MMP-9 concentration in the nucleus	
$r_{exp}$	Experimental calcification rate	
$R_{sim}$	Model calcification rate	
$oldsymbol{\phi}_{\scriptscriptstyle D-N}$	Fraction of nodule surface area in contact with dead cells	
η	Calcification rate adjusting factor	

Experimental models of CAVD, both in vitro, ex vivo, and in vivo, have identified several signaling pathways that contribute to CAVD pathophysiology, including the bone morphogenic protein (BMP), Notch1, wingless-related



Abnormal hemodynamic forces, such as shear stress, have been suggested as a potential driver for calcification, as they are known to cause tissue remodeling (Butcher et al. 2011, 2008; Balachandran et al. 2011). Studies conducted both in vitro and in vivo have shown that shear stress can activate latent TGF $\beta$  (Ahamed et al. 2008). Moreover, TGF $\beta$  has been identified as a key signaling pathway involved in EndMT (Dutta and Lincoln 2018), and is also responsible for upregulating matrix metallopeptidase 9 (MMP-9) (Kumarswamy et al. 2012). The increased levels of MMP-9 can lead to ECM degradation, thinning of the valve leaflets, loss of mechanical strength, and ultimately, valve dysfunction.

Valve disease research has traditionally relied on animal and static cell culture models. However, the emergence of organ-on-a-chip models, or microfluidic systems that integrate living cells to mimic multicellular architectures and organ functional units, has provided a new tool for studying tissue pathophysiology in vitro. Despite this, due to the enormous biological and biophysical complexity of cell-cell and cell-ECM interactions, it is challenging to experimentally decipher how multiple factors simultaneously contribute to calcification in aortic tissue. Therefore, mathematical and simulation tools have become increasingly important in the attempt to understand CAVD (Sadrabadi et al. 2021; Maleki et al. 2014; Weinberg and Kaazempur Mofrad 2007; Chandra et al. 2012; Arzani et al. 2017).

Most of the computational studies on CAVD reported in the literature utilized computational fluid dynamics (CFD) and fluid–structure interaction (FSI) methods. While these approaches are useful to evaluate aortic valve hemodynamics, they do not analyze cellular interactions and tissue remodeling processes (Mirza and Ramaswamy 2022; Sadrabadi et al. 2021; Amindari et al. 2017; Luraghi et al. 2019; Chandra et al. 2012). The focus of this study is to develop a new computational modeling framework for aortic valve calcification based on  $TGF\beta$  stimulation.

The progression of CAVD involves multiple scales spatially and temporally, with biochemical pathways occurring at the biomolecular and subcellular scales while tissue remodeling progresses at larger scale. Although developing multiscale models for simulating CAVD is challenging due to the complexity and uncertainty associated with the biological processes and the disparity between the modeling scales (Weinberg and Kaazempur Mofrad 2007; Bakhaty and Mofrad 2015), they can provide more comprehensive analysis about the progression of CAVD.



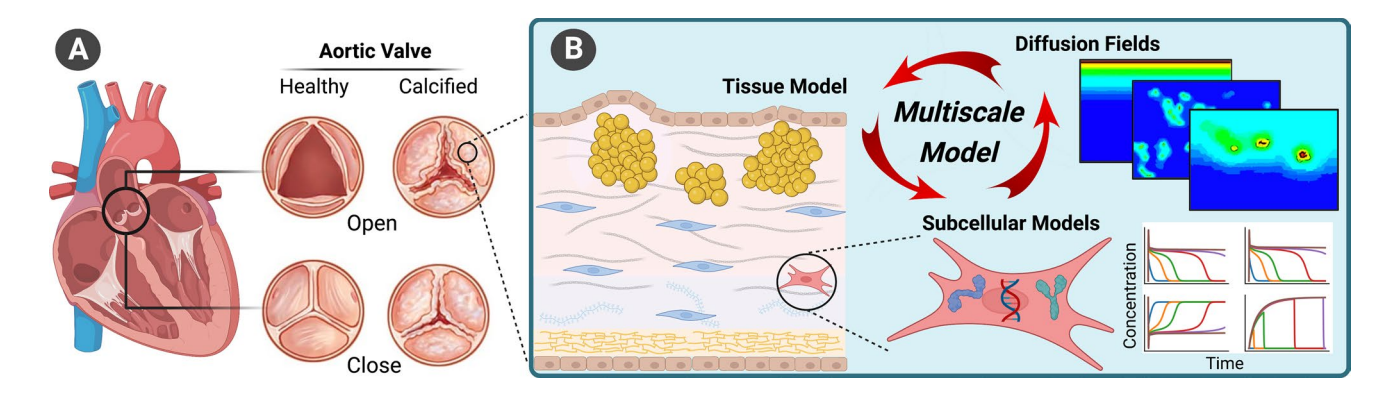


**Fig. 1** a schematic comparison between a healthy aortic valve and a calcified one, in both opening and closing states. **b** schematic illustration of our multiscale modeling framework, which consists of a tissue scale model, several diffusion fields, and subcellular models. Information is shared among different scales, where cells read cytokine concentrations from diffusion fields, and subcellular models generate

responses. The secretion and uptake of cytokines by cells are represented as sources and sinks in the diffusion fields. Tissue scale models implement cell-cell and cell-ECM interactions and processes such as fibrosis and calcification. Created with <a href="https://www.BioRender.com">https://www.BioRender.com</a>

One such model, developed by Arzani et al, simulates the cascade of mechanosensitive biochemical events that occur during aortic valve calcification (Arzani et al. 2017). The model combines a cell-scale systems biology model with organ-scale hemodynamics to study the trajectory of prominent biochemicals and cells involved in CAVD. The model comprises a system of ordinary differential equations that capture the effects of low-density lipoprotein (LDL) and  $TGF\beta$ . On the other hand, it does not simulate the interaction of cells and ECM or the progression of tissue remodeling in CAVD. Weinberg and Mofrad also examined the dynamic behavior of the human aortic valve at the cell, tissue, and organ length scales (Weinberg and Kaazempur Mofrad 2007). They linked simulations at different scales by applying deformations of one scale as boundary conditions to the other scales. While it provides insights into the mechanical properties and deformations of the tissue, it lacks cellular responses and systems biology analysis of the disease, which are critical to understanding the underlying factors for CAVD.

In this study, we aim to develop a novel multiscale modeling framework that integrates systems biology models with a tissue scale model to investigate the calcification process in CAVD. To achieve this, we incorporate the  $TGF\beta$  signaling pathway into the tissue-scale model cells that can undergo processes such as EndMT, cell differentiation, fibrosis, and calcification. This hybrid discrete-continuous modeling approach allows cells and fibers to interact in a discrete field, while the concentrations and transport of chemicals are modeled by solving ordinary differential equations (ODEs) and partial differential equations (PDEs). Although previous models have simulated aortic valve calcification (Arzani et al. 2017; Weinberg and Kaazempur Mofrad 2007), to the best of our knowledge, this is the first multiscale modeling

framework that incorporates cellular responses based on systems biology models within a discrete tissue model.

## 2 Methods

# 2.1 Model components

The multiscale modeling framework is composed of three major components: the subcellular TGF $\beta$  signaling pathway model, in which series of chemical reactions occur within each cell; diffusion fields in which proteins such as TGF $\beta$  and MMP-9 diffuse at the tissue model scale; and the tissue scale model in which cell-cell and cell-ECM interactions evolve and tissue remodeling occurs. Information between these components at different scales is shared to form a comprehensive framework (Fig. 1b).

# 2.2 Cellular Potts model

The primary component of the multiscale computational model is the Cellular Potts model (CPM) which was developed initially over thirty years ago (Graner and Glazier 1992). It stems from statistical mechanics models used to understand phenomena in solid-state physics. Since its inception, the CPM has been used in many studies to simulate individual biological cell behavior.

The full theoretical development of the CPM is well documented. There have been several computational implementations of the CPM. The most extensive computational framework is provided by the open source software platform CompuCell3D (Swat et al. 2012). The software has been used in a substantial number of published studies on cell and tissue behaviors and its implementation of the CPM is well verified.



Using Compucell3D, the CPM has been validated by simulations of in vitro observations of a variety of biological cell behavior (Jafari Nivlouei et al. 2022; Bustamante et al. 2021; Fortuna et al. 2020; Nguyen Edalgo et al. 2019; Kumar et al. 2016). Below we include a brief description of the physical basis of the approach.

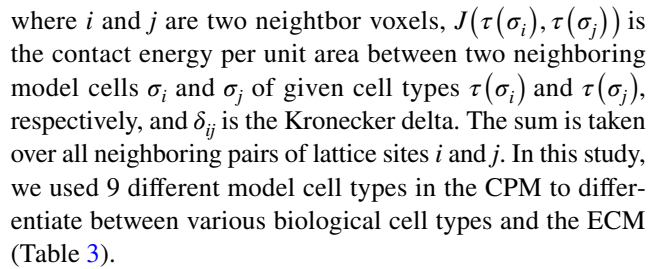
At the tissue scale, the CPM method is used for cell-cell and cell-ECM interactions and tissue remodeling. CPM is a lattice-based, multi-cell, and stochastic framework based on the Monte Carlo approach for tissue morphogenesis. Physiologically relevant simulations are based on a direct proportionality between Monte Carlo steps (MCSs) and physical time. In our simulations, each MCS is considered as one physical minute to match the physical cell time scale to the simulation time scale. The overall simulation duration is set to 14 physical days, mirroring the in vitro experimental time frame reported by Mendoza et al. (Mendoza et al. 2022). The whole simulation domain is divided into model cells (collection of voxels) and fiber bundles representative of the ECM. Specific biological cell types with distinct characteristics are assigned to the model cells. The dynamics of the CPM is governed by the Hamiltonian energy functionals, which describe the effective energy of a particular configuration of the model cells in the lattice. The effective energy is used to approximate biological constraints between model components, similar to that of the in vivo or in vitro biological systems. It consists of actual physical energies, such as cell-cell adhesion, along with terms that simulate energy-like effects, for instance a cell's chemotactic response to a concentration gradient in its surrounding (Keller and Segel 1971). By imposing constraints in the form of the effective energies, it becomes possible to simulate a wide range of cellular properties, including cell volume, membrane area, and more. In our simulation framework, three different terms contribute to the overall effective energy of a system, H:

$$H \equiv H_c + H_{cst} + H_m,\tag{1}$$

where  $H_c$  is contact energy associated with interactions between different entities,  $H_{cst}$  is constraint energy associated with change in cell shape and size, and  $H_m$  is energy related to cell motility.

Contact energies define the adhesive/repulsive dynamics of the model cell entities, and lower contact energies lead to stronger adhesion (e.g., higher concentration of membrane complex such as E-cadherin- $\beta$ -catenin binding (Ramis-Conde et al. 2008)) and vice versa. We denote  $\sigma_i$  as a generic cell that occupies the voxel i, and  $\tau(\sigma_i)$  as the cell type of the generic cell that occupies the voxel i. In the CPM the contact energy is defined as:

$$H_c = \sum_{i,j} J(\tau(\sigma_i), \tau(\sigma_j)) (1 - \delta_{ij}), \tag{2}$$



In the CPM, the absolute values of the contact energies are not as important as the hierarchy of contact energies between cells (Swat et al. 2012). We assume that the cells bind to each other more strongly than to the fibers (Chowkwale et al. 2019). Also, the microstructure of calcified nodules in our recent study shows that mineral structures are embedded within the fibrous collagen matrix, particularly localized around fiber bundles (Mendoza et al. 2022). Thus we use relatively lower contact energy for the nodule-fiber interaction. The contact energy per unit area hierarchy for our model is as follows:

$$J_{f-n} < J_{c-c} = J_{c-n} < J_{c-f}, (3)$$

where  $J_{f-n}$ ,  $J_{c-c}$ ,  $J_{c-n}$ , and  $J_{c-f}$  are the contact energy per unit area between fiber-nodule, cell-cell, cell-nodule, and cell-fiber, respectively. The values of the contact energies are determined by experimentation and chosen to keep the cell, nodule, and fiber bundle structures physiologically realistic and stable (summarized in Table 4).

Constraint energies in the CPM act like penalty functions which are minimized to satisfy the constraint. If the value of a parameter diverges from the pre-defined target value, the constraint energy increases. As the parameter value gets closer to the target value, the constraint energy approaches zero. The general form of constraint energy is expressed as

$$H_{cst} = \sum_{\sigma} \lambda_q(\tau(\sigma))[q(\sigma) - q_t(\tau(\sigma))]^2, \tag{4}$$

where q denotes the value of the quantity being analyzed,  $q_t$  signifies the target value for q, and  $\lambda_q$  represents the intensity or strength of the constraint for q. A large value of  $\lambda_q$ 

Table 3 List of model cell types used in this study

Model cell type	Explanation
qVEC	quiescent valvular endothelial cell
aVEC	activated valvular endothelial cell
qVIC	quiescent valvular interstitial cell
aVIC	activated valvular interstitial cell
OST	osteoblast-like cell
iFiber	initial fiber bundle
fFiber	fibrotic fiber bundle
DEAD	dead cell
CaNod	calcium nodule



Table 4 CPM parameter values

Parameter	Value	Comment
Temperature	100	Estimated
Monte Carlo Step	1 min	(Chowkwale et al. 2019)
Voxel (side)	2 μm	(Kumar et al. 2016)
Voxel (volume)	$8  \mu m^3$	(Kumar et al. 2016)
Lattice dimensions	$300 \times 100 \times 300$	Chosen
$J_{c-c}, J_{c-n}$	40	Estimated
$J_{c-f}$	200	Estimated
$J_{f-n}$	30	Estimated
$\lambda_v$ for qVEC	500	Estimated
$\lambda_{v}$ for aVEC, qVIC, OST	10	Estimated
$\lambda_{v}$ for DEAD	8	Estimated
$\lambda_{v}$ for iFiber, fFiber	15,000	Estimated
$\lambda_{v}$ for CaNod	2000	Estimated
$\lambda_{ch}$ for aVEC, aVIC, qVIC, OST	10000	Estimated
$\lambda_f$ for aVEC, aVIC	$-160 \sim 160$	Estimated

prevents q from significantly deviating from  $q_t$ . Because the CPM algorithm tries to minimize the effective energy of the system, it automatically drives any configuration toward one that satisfies the constraint.

Using this formulation, we employ a volume constraint for the model cells in the form of

$$H_{v} = \sum_{\sigma} \lambda_{v}(\tau(\sigma)) \left[ v(\sigma) - v_{t}(\tau(\sigma)) \right]^{2}, \tag{5}$$

where  $\lambda_{\nu}$  represents the intensity of the volume constraint,  $\nu$  denotes the volume of the model cell, and  $\nu_t$  signifies the target volume of the model cell. Lower values of  $\lambda_{\nu}$  makes the model cells more flexible for deformations and easier to migrate during the index-copying steps, while at higher  $\lambda_{\nu}$  values the cells are more rigid and more fixed in their positions. For instance, quiescent valvular endothelial cells

(qVECs) uniformly cover the surface layer of the tissue, and thus we use relatively high value of  $\lambda_{\nu}$  to constraint them to their initial positions during the simulation. In contrast, a lower  $\lambda_{\nu}$  value is suitable for dead cells because they can easily change form and disintegrate into apoptotic fragments (Table 5).

The process of calcium nodule (CaNod) nucleation begins with the random generation of a single voxel around osteoblastic-like cells (OSTs). Over time, the calcium nodules gradually increase in size. The width of the fiber bundles is limited to a single voxel. These small entities are prone to deletion by index copy attempts and thus a higher  $\lambda_{\nu}$  value is assigned to prevent such occurrence. Trial testing showed that  $\lambda_{\nu} = 2000$  for the calcium nodules and  $\lambda_{\nu} = 15,000$  for fiber bundles will prevent undesirable index copies and ensure their existence.

Table 5 Diffusion parameters

Parameter	Value	Comment
D (MMP-9)	6 μm <sup>2</sup> /min	Computational (Collier et al. 2011; Kumar et al. 2016; Anderson 2005; Franssen et al. 2019)
k (MMP-9)	$0.0048 \; \mathrm{min^{-1}}$	Empirical (Chowkwale et al. 2022)
$s_0$ (MMP-9)	$1.2 \times 10^{-11} \text{nM/(cell min)}$	Empirical (Chowkwale et al. 2022)
γ (MMP-9)	$1.5 \times 10^{-12}$	Empirical (Chowkwale et al. 2022)
$D (TGF\beta)$	$186  \mu m^2 / min$	Empirical (Son et al. 2017)
$k \text{ (TGF}\beta)$	$0.22 \; min^{-1}$	Empirical (Wakefield et al. 1990)
$s$ (TGF $\beta$ )	$3.5 \times 10^{-11} \text{nM/(cell min)}$	Empirical (Chowkwale et al. 2022)
TGF $\beta$ input concentration	0.001 to 0.1 nM	Empirical (Ahamed et al. 2008; Abdelhalim 2011)
D (Fiber)	2 μm <sup>2</sup> /min	Estimated
k (Fiber)	0.5 min <sup>-1</sup>	Estimated
Pseudo-concentration value for a fiber bundle	1 (arbitrary unit)	Assumed pseudo-parameter



The last contributing energy term,  $H_m$ , accounts for the motility of the model cells due to chemotaxis and other directional movements. While cell migration is a complicated process, in computational models it can be represented as a random walk (Thampatty and Wang 2007). We incorporated an energy associated with chemotaxis of model cells toward collagen fibers (O'Brien et al. 2010),  $H_{ch}$ , and a random force  $H_f$  was additionally applied to model cells exhibiting higher motility characteristics, such that

$$H_m = H_{ch} + H_f. ag{6}$$

Chemotaxis is expressed in the form of a change in energy:

$$\Delta H_{ch} = -\lambda_{ch}(c(i) - c(j)),\tag{7}$$

where  $\lambda_{ch}$  the strength and direction of chemotaxis, and c(i) and c(j) are the concentration field values of target voxel and source voxel, respectively, during index-copy attempts. Fiber bundle interaction tests showed that with  $\lambda_{ch} = 10000$  cells become attracted to the fiber bundles in their surroundings. Low  $\lambda_{ch}$  values hinder cell-fiber interaction, promoting straight cell movement, while high  $\lambda_{ch}$  values cause cells to bind strongly to fibers, impeding movement and causing them to get stuck easily. For cells with higher migratory properties, an additional force is incorporated in the form of

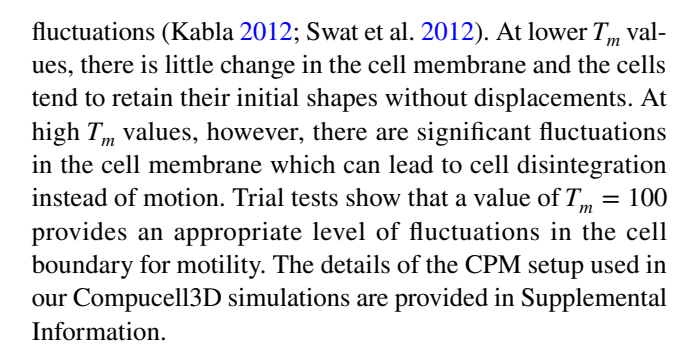
$$\Delta H_f = -\lambda_f(p(i) - p(j)),\tag{8}$$

where  $\lambda_f$  the strength and direction of the force, and p(i) and p(j) are the positions of target voxel and source voxel, respectively, during index-copy attempts. Assuming a maximum velocity of  $0.3 \, \mu \text{m/min}$  for the cells (Kick et al. 2016), the cell velocity trial tests indicated that the maximum  $\lambda_f$  value that could be employed would be approximately 160. The value of  $\lambda_f$  for the activated cells is determined by its proportionality to the concentration of the  $\alpha \text{SMA}$  protein in the subcellular model, a known indicator of increased migratory potential in myofibroblasts (Kawamoto et al. 1997). The sign of the force is chosen randomly in three dimensional space to generate random walk behavior in the simulation.

In the CPM the model cells move their boundaries by emulating cytoskeletally driven cell motility through index copy attempts that change the effective energy. These attempts are stochastically accepted or rejected with a probability that depends on the resulting change of the overall effective energy *H* based on the Boltzmann acceptance function (Chen et al. 2007):

$$P(\sigma_i \to \sigma_j) = \begin{cases} e^{-(\Delta H/T_m)} & \text{if } \Delta H > 0\\ 1 & \text{if } \Delta H \le 0 \end{cases}$$
 (9)

where  $T_m$  does not reflect any conventional thermal temperature; instead, it represents the strength of noise in the dynamics and can be regarded as the amplitude of cell-membrane



# 2.3 Diffusion fields

The CPM methodology can be extended to include other physical components such as diffusion fields, which can be utilized to simulate the secretion, uptake, and transport of cytokines within the domain (Swat et al. 2012). Here, three separate diffusion fields are included:  $TGF\beta$ , MMP-9, and fiber bundles. These fields are governed by the diffusion equation

$$\frac{\partial c}{\partial t} = D\nabla^2 c - kc + s,\tag{10}$$

where c is the field concentration and D, k and s denote the diffusion coefficient, decay constant and secretion rate, respectively.

A Dirichlet boundary condition is set at the surface of the qVEC (i.e., the blood vessel lumen) with a fixed value of 0.08 nM for the TGF $\beta$  concentration, while zero gradient Neumann boundary conditions are imposed on the other boundaries of the tissue domain. The diffusion coefficient and decay rate for active TGF $\beta$  are set to be 186  $\mu$ m<sup>2</sup>/min and 0.22 min<sup>-1</sup>, respectively (Son et al. 2017; Wakefield et al. 1990). Upon activation, cells secrete TGF $\beta$  at a rate of  $3.5 \times 10^{-11}$  nM/(cell·min) (Chowkwale et al. 2022). MMP-9's diffusion coefficient and decay rate are 6 μm<sup>2</sup>/min and 0.0048 min<sup>-1</sup>, respectively (Collier et al. 2011; Kumar et al. 2016; Anderson 2005; Franssen et al. 2019). Since only activated cells within the tissue secrete MMP-9, we apply zero gradient at all tissue boundaries. While an MMP-9 secretion rate of  $1.2 \times 10^{-11}$  nM/(cell·min) has been suggested in the literature (Chowkwale et al. 2022), we allow the cells to secrete MMP-9 at a rate that is linearly proportional to the MMP-9 concentration in the nucleus from the subcellular model.

$$s = s_0 \left(\frac{c_n}{c_0}\right) \tag{11}$$

where  $s_0 = 1.2 \times 10^{-11}$  nM/(cell·min),  $c_n$  is the concentration in the nucleus, and  $c_0 = 8.3$  nM is the maximum MMP-9 concentration value attainable in the subcellular model (as shown in Fig. 3).



The cells in tissues are anchored to collagenous structures, indicating a higher adhesion between cells and fibers (Heino 2007). However, applying a lower contact energy in the CPM method does not realistically simulate the obstruction of fibers when cells move past them, as it results in a higher index copy acceptance when cells come in contact with fibers. To overcome this, we considered a higher contact energy between cells and fibers and model the propensity of cells to attach to fiber bundles by dedicating a pseudo-diffusion field for fiber bundles to attract cells toward the fiber bundles through chemotaxis. This agrees with previous work that has shown collagen to have chemoattractant properties (O'Brien et al. 2010). To ensure the effectiveness of chemotaxis and avoid interference with nearby fiber bundles, we assumed a diffusion coefficient of 2 µm<sup>2</sup>/min and a decay rate of 0.5 min<sup>-1</sup> for this field, which results in a range of two to four voxels with a nonzero local pseudoconcentration gradient. Additionally, we used a fixed constant concentration value of unity as a boundary condition for all fiber bundles and set all tissue domain boundaries to a zero gradient boundary condition. By combining an overall attraction of the cells to the fibers and a low probability of index copy acceptance of cells to the immediately adjacent fiber bundle voxels, we can simulate realistic cell movement behavior around the fibers.

## 2.4 Calcification model

**EndMT:** Endothelial-to-mesenchymal transition (EndMT) is an intricate cellular differentiation process whereby endothelial cells lose endothelial markers like platelet endothelial cell adhesion molecule-1 (PECAM-1) and detach and migrate into the deeper parts of the tissue and express mesenchymal markers such as alpha smooth muscle actin ( $\alpha$ -SMA). Previous studies showed that the EndMT and epithelial-to-mesenchymal transition (EMT) are key regulators in diseases such as kidney fibrosis, cancer and cardiovascular diseases (Dongre and Weinberg 2019) (Sánchez-Duffhues et al. 2018). Accumulating evidence indicates that EndMT plays a role in the pathogenesis of CAVD (Mahler et al. 2013) (Ma et al. 2020) .

In our model, the top layer of the simulated tissue is covered by quiescent valvular endothelial cells (qVECs), which can become stimulated based on the amount of  $TGF\beta$  in their surroundings (Fig. 2). Experimental studies have shown that approximately 1% of valvular endothelial cells (VECs) undergo the EndMT process in healthy valves, and upon  $TGF\beta$  stimulation. However, However, up to 9% of endothelial cells can undergo EndMT (Bischoff 2019). In our model, we assume that 5% of eligible VECs, determined based on their PECAM-1 protein levels, undergo the EndMT process. The PECAM-1 protein level in the subcellular model is utilized to trigger the transition from the qVEC to the activated

valvular endothelial cell (aVEC) state, where the threshold for activation of VECs is set to half of the initial PECAM-1 level. Furthermore, aVECs can return to the quiescent state if the PECAM-1 level falls below the threshold, except in the case of a prolonged activity of the aVEC defined by a continuous active time period exceeding 48 h (Chowkwale et al. 2019).

Quiescent valvular interstitial cells (qVICs) are randomly scattered inside the tissue and can be activated by the TGF $\beta$ protein (Fig. 2). We use the  $\alpha$ SMA protein level from the subcellular models for activation and deactivation of VICs to switch the state from qVIC to aVIC and vice versa. The threshold for activation of VICs is set to half of the maximum  $\alpha$ SMA concentration, which is 4.2 nM. Moreover, aVICs can return to the quiescent state if the concentration of  $\alpha$ SMA drops below the threshold, unless the duration of activity exceeds 48 h (Chowkwale et al. 2019). aVECs and aVICs exhibit fibrosis activity by depositing collagen fiber bundles at a rate of  $3.2 \times 10^{-10}$  mg/(cell.min) (Kumarswamy et al. 2012; Masur et al. 1996; O'Brien et al. 2005). They are also programmed to exhibit a higher migratory property that is proportional to the concentration of  $\alpha$ SMA in the subcellular calculations.

Shear stress to  $TGF\beta$  concentration: Studies conducted both in vivo and in vitro have shown that shear forces can trigger the activation of latent TGF $\beta$  in blood (Ahamed et al. 2008). Excessive or abnormal mechanical stress can also trigger the activation of latent TGF $\beta$  within the tissue by disrupting its complex, thus releasing active  $TGF\beta$  into the tissue (Sarper et al. 2016; Dayawansa et al. 2022). In this study, for model simplicity we are solely addressing  $TGF\beta$ activation through blood shear stress, while postponing the consideration of TGF $\beta$  activation within the tissue induced by mechanical stress to future model development. By utilizing shear stress and shear rate conversion methods (Abdelhalim 2011), we can determine the concentration of active TGF $\beta$ . For instance, a shear stress of 20 dyne/cm<sup>2</sup> (Butcher et al. 2006; Mendoza et al. 2022) is indicative of active TGF $\beta$  concentrations of approximately 0.08 nM, which is used as a boundary condition for TGF $\beta$  diffusion field in the tissue model.

Cell Death: Fibrotic activity results in stiffening of the heart valve, reduced nutrient diffusion, and eventually leads to cell death (Piek et al. 2016). In our model, we determine necrosis by measuring fraction of the cell surface area exposed to the medium, and if this fraction drops below 10%, the model cell dies and changes type to dead cell (DEAD). Furthermore, if a cell become trapped in an area with a high level of fibrosis or calcification and its mobility is limited, cell death is likely to occur (Fig. 2). We assess the intensity of fibrosis with the fiber field value and use 75% of the maximum fiber field value as a threshold. For cells trapped in calcified or fibrotic regions, we use a cell



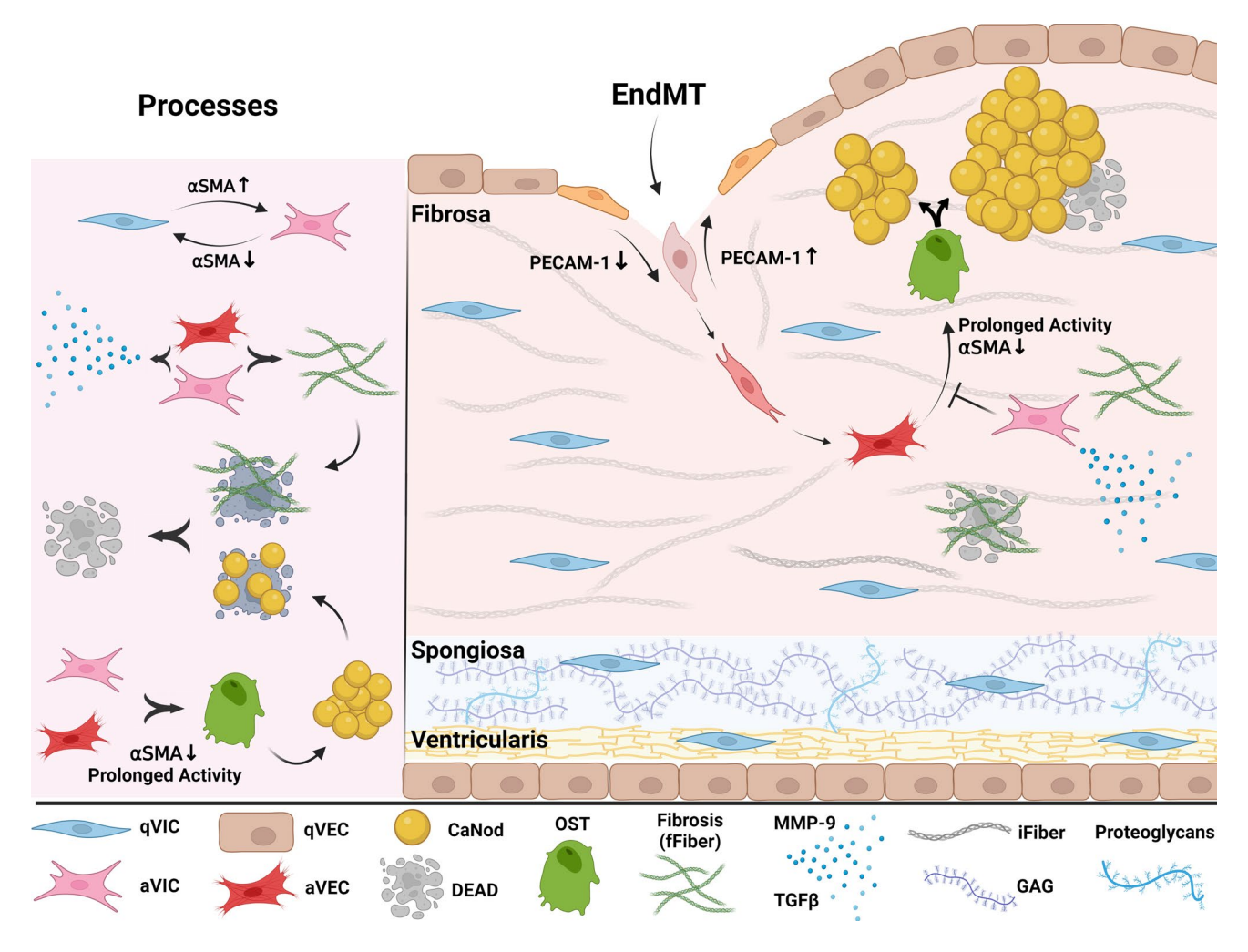


Fig. 2 Schematic illustration of the tissue model consisting of three layers: the Fibrosa, Spongiosa, and Ventricularis layers. The Fibrosa layer is the outermost layer of the valve, covered by qVECs, and primarily composed of collagen fibers. The Spongiosa layer is the middle layer of the valve and mainly composed of proteoglycans and glycosaminoglycans (GAGs). The Ventricularis layer is the innermost layer of the valve, predominantly composed of elastic fibers and covered by qVECs. qVECs can undergo EndMT transition upon PECAM-1 downregulation, becoming aVECs, while qVICs can be

activated by upregulating aSMA and becoming aVICs. Both aVECs and aVICs secrete MMP-9 and TGF $\beta$  and deposit fFibers during the fibrosis process. Prolonged activity and downregulation of aVECs and aVICs can lead to differentiation into OSTs, resulting in calcium nodule nucleation and growth. VICs can inhibit the differentiation of aVECs into OSTs when they are in close proximity. Cells can die by becoming trapped in high fibrotic or calcified areas, and the resulting dead bodies can act as feeding sites for CaNods. Created with https://www.BioRender.com

velocity threshold of  $0.003~\mu m/min$  (1% of the maximum cell velocity) for determining insignificant cell movement (Nekolla et al. 2016).

Osteoblastic differentiation: Interstitial cells in the valve undergo osteoblastic differentiation in response to  $TGF\beta$  (Osman et al. 2006). An experimental study by Hjortnaes et al. showed that osteogenic differentiation markers such as Runx2, osteopontin and osteocalcin significantly increase, and EndMT markers such as  $\alpha$ SMA expression decreases in osteoblastic-like interstitial cells (Hjortnaes 2015). Therefore, osteoblastic differentiation is modeled when activated cells exhibit prolonged activity and  $\alpha$ SMA concentration starts to decrease. Additionally, Hjortnaes et al. suggested

that VICs inhibit the osteogenesis of VECs (Hjortnaes 2015). To model this inhibitory behavior, the surface area of each aVEC is examined before differentiation to the osteoblastic-like type, ensuring that there is no contact between aVECs and VICs.

Calcification: Both ossification and dystrophic calcification have been theorized to contribute to the calcification of the valve tissue. In the active ossification, the osteogenic differentiation of the interstitial cells give rise to the calcific nodules. (Masjedi et al. 2017). To simulate this process in the computational model, OST cells are coded to initiate calcification nucleation. In the passive dystrophic calcification, dead and damaged interstitial cells are a significant source of



calcium deposits and calcification and form calcific nodules (Steitz et al. 2002; Butcher et al. 2011). In the computational model this process is captured by the setting that, when a calcified nodule is in contact with DEAD cells, the DEAD cells are considered as feeding sites and the calcification rate for the nodule would increase based on the nodule surface ratio in contact with the DEAD cells. Based on our in vitro study, we calculated the experimental calcification rate  $r_{\rm exp}$  to be 0.1  $\mu {\rm m}^3/({\rm min} \cdot {\rm nodule})$ , assuming a constant rate over the course of the experiment (Mendoza et al. 2022).

In order to incorporate the influence of different sources on the calcification rate, we make an assumption that approximately half of the calcification rate is attributed to the proximity of DEAD cells, while the other half is dependent on other biological processes not captured in our model. Leveraging the in vitro data, we express the model calcification rate  $R_{\rm sim}$  as

$$R_{\text{sim}} = \frac{r_{\text{exp}}}{2} \phi_{\scriptscriptstyle D-N} \eta + \frac{r_{\text{exp}}}{2},\tag{12}$$

where  $\phi_{\scriptscriptstyle D-N}$  represents the fraction of a CaNod surface area that is in contact with DEADs, and  $\eta$  is an adjustable weighting factor. The range of  $\phi_{\scriptscriptstyle D-N}$  is between 0 and 1, where 0 indicates no surface area in contact with any DEADs, and 1 indicates the entire nodule surface is surrounded by DEADs. Since  $r_{\rm exp}$  represents a target calcification rate for a CaNod, through trial-and-error we have found that  $\eta=10$  provides a reasonable result for  $R_{\rm sim}$ .

Table 6 summarizes all parameter values used in our simulations.

# 2.5 TGF $\beta$ signaling pathway

The TGF $\beta$  signaling pathway is used in the subcellular modeling within each model cell and is integrated with the CPM and the rest of the simulation framework. In Supplemental Information, the model details are provided in Antimony language (Chowkwale 2019). The TGF $\beta$  concentration from the diffusion field is used as an input for the subcellular model in each cell. The values of PECAM-1 and  $\alpha$ SMA obtained in the subcellular models are used for cell type differentiation, and if cells are activated, MMP-9 and TGF $\beta$ proteins are secreted into their surroundings in the diffusion fields. The subcellular models are deterministically solved using libRoadRunner, which is a simulation engine in a C++ library used for simulating and analyzing systems of differential equations (Welsh et al. 2023). The CVODE integration method is chosen, which uses a backward differentiation formula solver for stiff ODE problems.

# 2.6 ECM and tissue composition

The noncellular portion of connective tissues is known as the extracellular matrix (ECM), a complex meshwork of insoluble fibrillar proteins and signaling factors interacting together to provide physical scaffolding and instructional

Table 6 Model parameter values

Parameter	Value	Comment
Initial VIC density	10 <sup>7</sup> cell/ml	Empirical (Mendoza et al. 2022)
Initial VEC density	106 cell/cm <sup>2</sup>	Empirical (Mendoza et al. 2022)
Initial collagen concentration	1.5 mg/ml	Empirical (Mendoza et al. 2022)
Collagen fiber density	1.3 mg/ml	Empirical (O'Brien et al. 2005)
Fibrosis rate	0.32 pg/(cell·min)	Empirical (Kumarswamy et al. 2012; Masur et al. 1996; O'Brien et al. 2005)
Calcification rate	0.1 μm <sup>3</sup> /(min·nodule)	Empirical (Mendoza et al. 2022)
MMP-9 threshold for fiber degradation	$3.6 \times 10^{-11} \mathrm{nM}$	Computational (Chowkwale et al. 2022)
Cell doubling time	1800 min	Empirical (Rush 2018; Pho et al. 2008)
Maximum cell velocity	0.3 μm/min	Empirical (Nekolla et al. 2016)
Initial cell size	$10\mu\text{m}\times10\mu\text{m}\times10\mu\text{m}$	Empirical (Bosse et al. 2013)
Fiber bundle length	50 μm	Computational (Lee et al. 2014; Kumar et al. 2016)
Fiber bundle thickness	2 μm	Computational (Kumar et al. 2016)
Fiber field criterion for cell death	> 75%	Assumed: 75% of parameter range
Medium exposure criterion for cell death	< 10% of cell surface area	Assumed: 10% of parameter range
Medium Exposure criterion for cell growth and mitosis	> 50% of cell surface area	Assumed: average of parameter range
$\alpha$ SMA field threshold for VIC activation	4.2 nM	Assumed: average of parameter range
Velocity criterion for insignificant movement leading to cell death	< 0.003 μm/min	Empirical (Nekolla et al. 2016)
EndMT-derived activation rate of qVECs	1 to 10%	Empirical (Bischoff 2019)



cues to the surrounding cells. In our modeling framework, the ECM is modeled as randomly generated fiber bundles within the domain, which contains several diffusion fields responsible for transporting signaling proteins. In the aortic valve fibrosa collagen I is the most abundant ECM protein (Taylor 2007), and since it has a typical length of 20-200 µm and a typical thickness of 200-350 nm (Lee et al. 2014), we chosen each fiber bundle in our model to be 50 µm in length and 2 µm in thickness similar to those used by (Kumar et al. 2016). By assuming a collagen concentration of 1.5 mg/ml as in the previously reported in vitro experiment (Mendoza et al. 2022) and a collagen fiber density of 1.3 mg/ml (O'Brien et al. 2005), we determined and set the number of fiber bundles in our computational tissue domain. Two types of fiber bundles, iFiber and fFiber, are specifically defined to differentiate between the fiber bundles that already exist at the start of the simulation (iFiber) and the fiber bundles that are formed during fibrosis simulations (fFiber).

At the start of the simulation, the tissue consisted of only qVECs, qVICs, and iFibers. The cells are assumed to be cubic in shape with dimensions of  $10 \, \mu m$ . The qVECs cover the top part of the tissue with a concentration of  $10^6$  cell/cm², assuming confluency. qVICs, on the other hand, are randomly scattered within the ECM with a concentration of  $10^7$  cell/cm³ (Mendoza et al. 2022).

## 2.7 Fibrosis

Fibrosis is typically caused by the abnormal accumulation of ECM components, particularly collagen, within tissues. The presence of fibrosis is associated with calcification and contributes to valve obstruction, as evidenced by contrast-enhanced CT and histology images (Cartlidge et al. 2021). It is known that  $TGF\beta$  can induce fibrosis through myofibroblast activation which results in excessive production of ECM components (ming Meng et al. 2016). The typical collagen concentration in a heart valve is around 5 mg/ml, which can increase up to 13 times due to fibrosis induced by TGF $\beta$  (Kumarswamy et al. 2012). Moreover, the cell concentration in a typical heart ranges from 0.5 to  $1 \times 10^8$  cells/cm<sup>3</sup>, and about 5% of the cells undergo myofibroblast differentiation upon TGF $\beta$  stimulation (Masur et al. 1996). Using these data, we estimated the fibrosis rate in the heart valve to be approximately  $3 \times 10^{-10}$  mg/(cell·min). In our simulation model, once cells become activated they initiate fibrosis by randomly generating fiber bundles around them. Using a fiber density of 1.3 g/ml (O'Brien et al. 2005), the model calculates the fiber bundle volume and generates fiber bundles accordingly, with a maximum bundle length of 50 µm and a bundle thickness of 2 μm.



In addition to synthesizing collagen, myofibroblasts are also the primary source of MMPs that degrade matrix proteins (Horn and Trafford 2016). Activated cells in the model start secreting matrix degrading enzymes based on the concentration of MMP-9 protein in the subcellular model calculations. Upon secretion, MMP-9 molecules diffuse throughout the ECM. If the concentration of MMP-9 around a fiber bundle exceeds a certain threshold, degradation of the fiber bundle is initiated. We set the threshold to be  $3.6 \times 10^{-11}$  nM, which is three times the maximum secretion concentration of MMP-9 by activated cells (Chowkwale et al. 2022).

## 2.9 Mitosis

Mitosis is a process of cell duplication during which one cell splits into two genetically identical daughter cells. Nutrients are essential for cell growth and DNA synthesis in mitosis (Gottesman 2014). In our model, we approximate a cell's access to nutrients by calculating the fraction of the cell's surface area in contact with the medium. If this fraction is more than 50%, the cell will grow and proceed with the mitosis process. Reported experimental studies showed that the doubling time for myofibroblast with higher expression of  $\alpha$ SMA in heart valve interstitial cells is around 30 h (Rush 2018; Pho et al. 2008). Thus, we use this value for mitosis of activated cells when they have access to enough nutrients in their surroundings.

## 3 Results and discussion

## 3.1 Subcellular model

The concentrations of PECAM-1, αSMA and MMP-9 were used in our subcellular model. PECAM-1 helps distinguish between qVEC and aVEC, MMP-9 is responsible for the degradation of ECM, and  $\alpha$ SMA plays a role in the differentiation to OST and in the change of cells between the quiescent and the activated states. Depending on the local TGF $\beta$  concentration as an input to the subcellular model, cells may exhibit varying behaviors. Quiescent cells with less movement receive TGF $\beta$  similar to a continuous input while activated cells with higher migratory properties experience a TGF $\beta$  field similar to an initial input at the beginning when moving toward lower concentrations. Although the cells may experience  $TGF\beta$  as a combination of an initial input and continuous inputs, analyzing the subcellular model separately helps associate input types with cell behaviors. The results of the TGF $\beta$  subcellular model for an initial input and continuous inputs at different concentration levels are shown in Fig. 3.



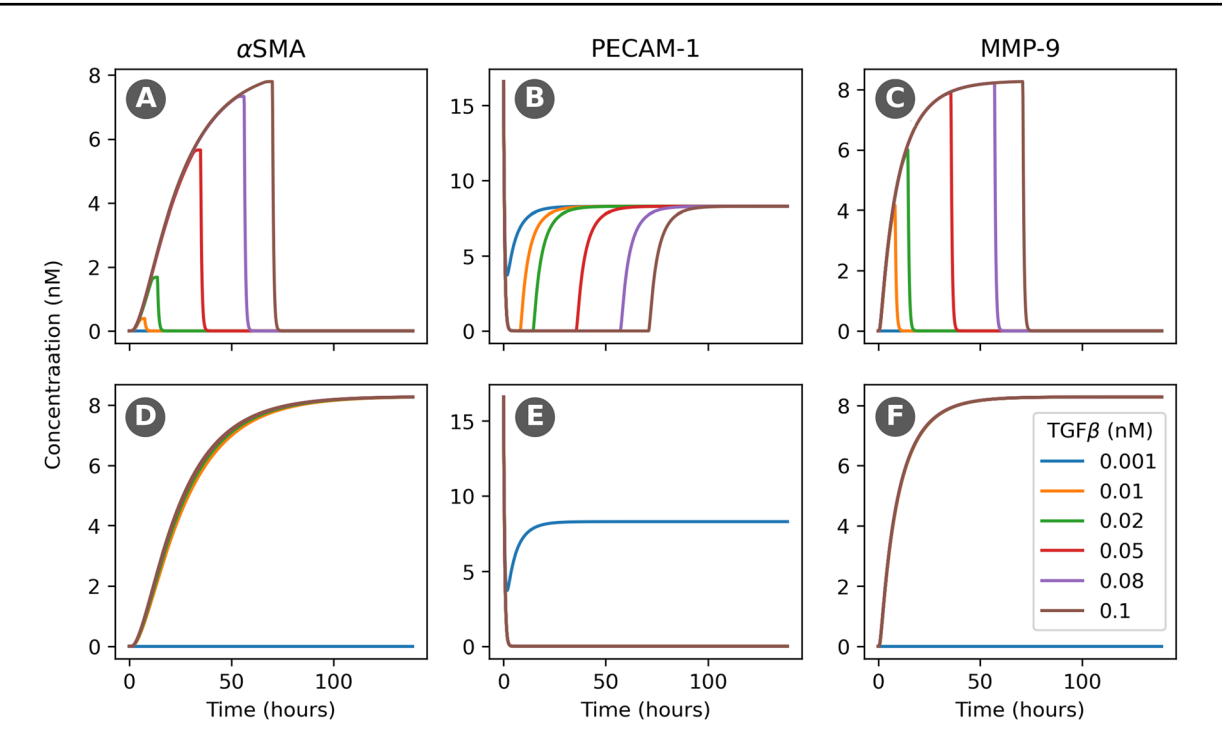


**Fig. 3** Subcellular model responses with different concentration levels of  $TGF\beta$  and input types. The first row **a–c** are protein concentrations with a  $TGF\beta$  input pulse at the start of the simulation (Time = 0 h). The second row **d–f** are protein concentrations under a continu-

ous TGF $\beta$  input since the start of the simulation. **a** and **d** are concentrations of  $\alpha$ SMA. **b** and **e** are concentrations of PECAM-1. **c** and **f** are concentrations of MMP-9

It is found that higher TGF $\beta$  concentrations increase  $\alpha$ SMA and MMP-9 concentration levels, while decreasing PECAM-1 protein. In the case of an initial input (Fig. 3a–c), higher TGF $\beta$  concentrations intensify and prolong protein expression, which are characteristics of activated cells. Except for very low concentrations of TGF $\beta$  that are insufficient to trigger pathway reactions, all protein expressions follow a similar pattern with different active time scale even under varying TGF $\beta$  concentration levels. In the case of continuous inputs of TGF $\beta$  (depicted in Fig. 3d–f), the protein expressions exhibit a consistent pattern across different levels of TGF $\beta$  concentration, with the exception of very low concentrations that are not enough to initiate pathway reactions. The subcellular models provide protein concentration values for each cell, which are utilized to assess the cells' states and guide their differentiation, mirroring their behaviors observed in in vitro studies.

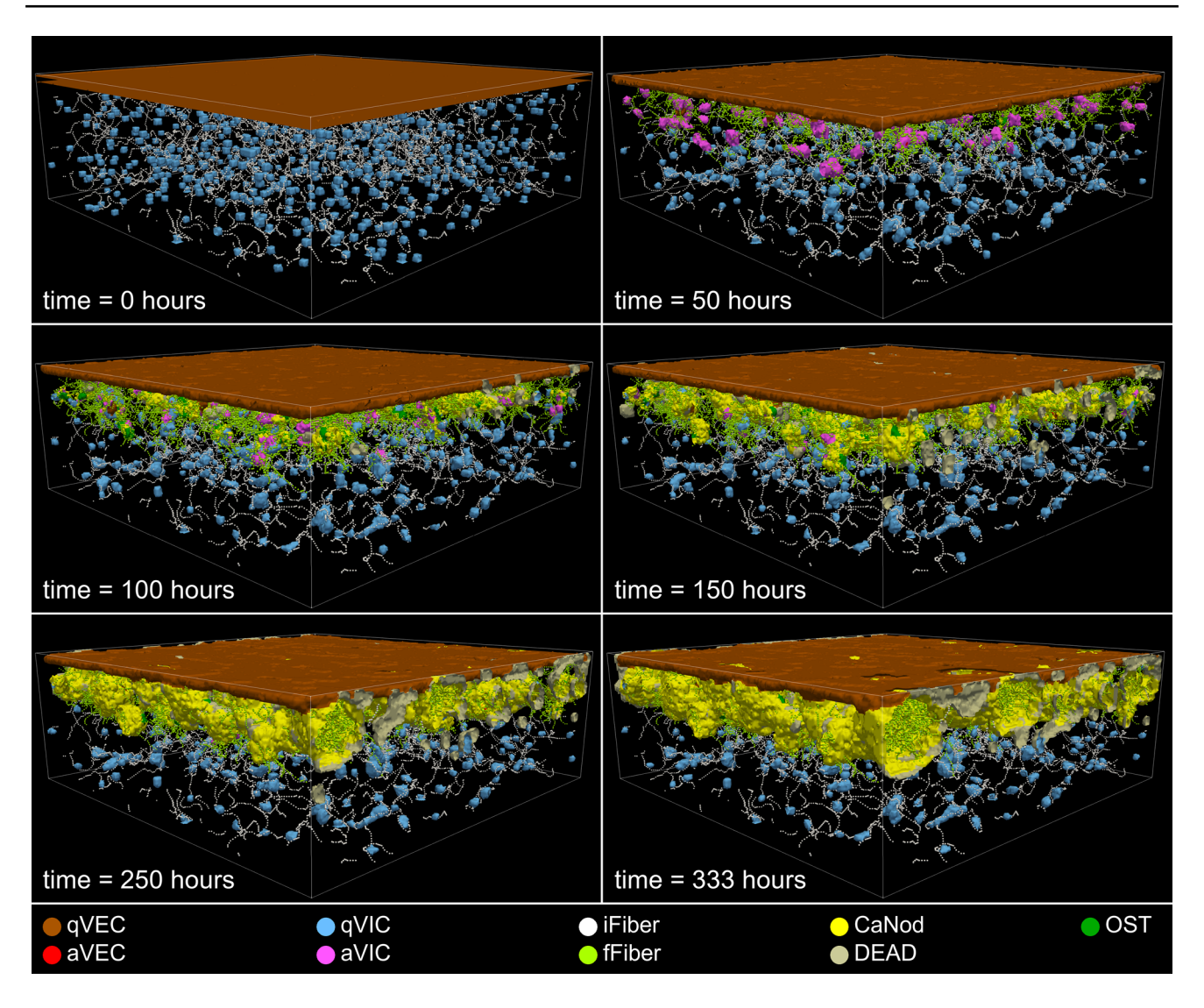
# 3.2 Tissue model

Figure 4 presents snapshots of the tissue taken at various time instances after the start of the simulation. At the outset of the simulation, the top layer of the domain is covered by qVECs while qVICs are dispersed inside. Initial fiber bundles are created and randomly oriented throughout the domain. As the simulation progresses, quiescent cells can

become activated from being exposed to  $TGF\beta$  and begin to produce matrix-degrading enzymes (MMP-9). They can also move more quickly and deposit collagen fiber bundles, resulting in fibrosis. At the 50-hour mark, an early stage of fibrosis is visible, as illustrated by activated cells having deposited fiber bundles colored in light green (Fig. 4). Exposure of activated cells to lower concentrations of TGF $\beta$ can revert the cells back to the quiescent state. However, prolonged status as activated cells can trigger their differentiation into OSTs, which initiate the calcification process. An early stage of calcification can be observed in Fig. 4 at the 100-hour mark. Moreover, higher fiber deposition at that time stimulates cell death in highly fibrotic regions. As nodules continue to grow, more cells die, which in turn further elevates the nodules' growth rate. Eventually, the majority of cells in highly fibrotic or calcified regions are dead, as depicted in Fig. 4 at 333 h. To provide a more detailed visualization of the tissue remodeling, we created separate figures for VICs, VECs, OSTs, DEADs, iFibers, fFibers, as well as diffusion fields associated with MMP-9 and TGF- $\beta$ . These additional figures can be found in the Supplemental Information section.

Activated fibroblasts or myofibroblasts are characterized by their increased expression of ECM proteins and fibrogenic cytokines, which contribute to the mechanical properties of affected tissues (Phan 2008). In CAVD, osteogenic





**Fig. 4** Remodeling of the tissue at different time points. Different cell types, fibers and nodules are presented in different colors. Brown, red, blue, and pink are related to qVEC, aVEC, qVIC, and aVIC, respec-

tively. Initial fiber bundles are white and fibrotic fiber bundles are light green. Calcium nodules, dead cells and osteobalst-like cells are yellow, gray, and dark green, respectively

differentiation has been observed, and dead cells are a major source of calcification (Steitz et al. 2002; Butcher et al. 2011). Thus, tracking the population of cell types during tissue remodeling is crucial for understanding disease progression and developing potential treatment methods. However, monitoring cells' differentiation steps experimentally can be difficult, and this is where computational models are beneficial. By keeping a record of each cell's evolutionary path, these models can provide insight into the dynamics of tissue remodeling.

In this simulation, cell differentiation into various types was counted and presented in Fig. 5 as a fraction of all cells during the simulation. The results indicate that approximately 9.6% of all quiescent cells became activated, of which about 4.7% returned to the quiescent state. A smaller

proportion of a VECs became quiescent compared to a VICs, which could be due to the exposure of VECs to higher  $TGF\beta$  concentrations near the boundary while the VICs were exposed to lower  $TGF\beta$  concentrations at deeper parts of the tissue. Depending on the protein concentration, activated cells can differentiate into osteoblast-like cells, return to the quiescent state, or become trapped among calcified nodules or fibrotic fibers and die.

During the simulation, it was observed that about 7.4% of the activated cells differentiated into osteoblast-like cells, which initiated the formation of calcified sites around them. As time passed, these sites grew in size, and the osteoblast-like cells became trapped inside them. Eventually, the majority of these cells died due to a lack of nutrients. Overall, the simulation showed that 21.8% of the cells died, getting



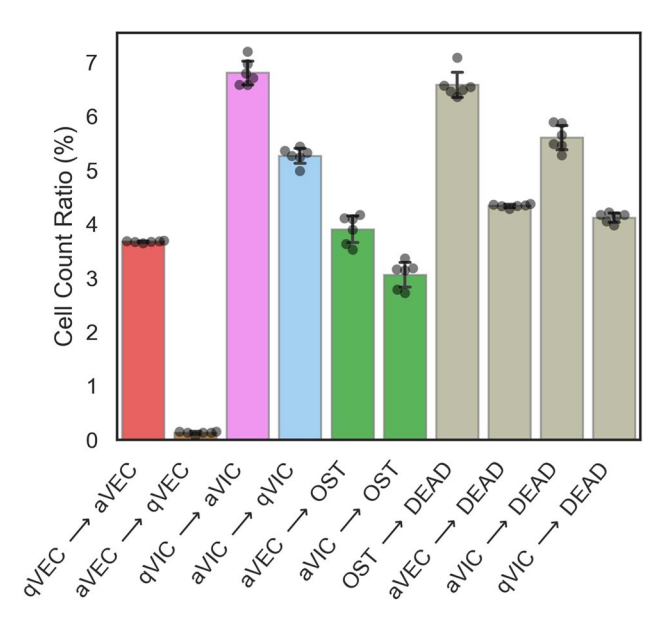


**Fig. 5** Cells phenotype transition during the simulation from six simulation runs with different random seedings

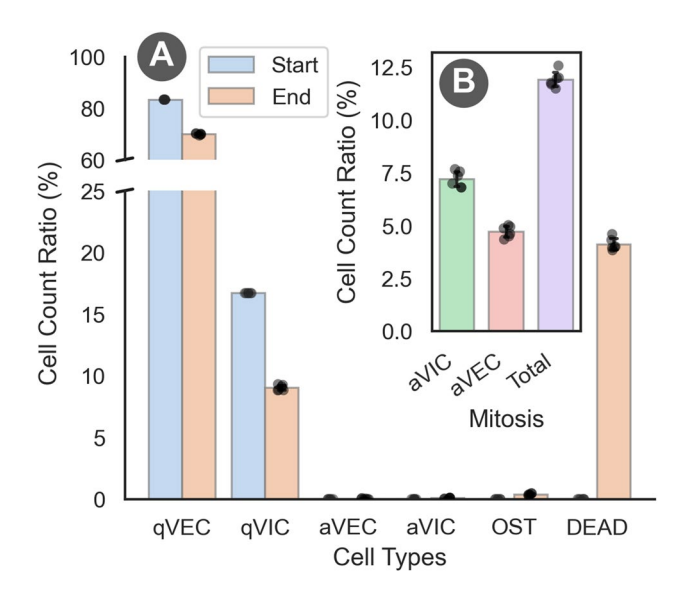


**Fig. 6** Cell count statistics from six simulation runs with different random seedings. **a** Cell count ratio comparison for different types at the start and end of the simulation. **b** Generated cells due to the mitosis activity of aVIC and aVEC

trapped in either fibrotic or calcified areas (Fig. 5). The apoptotic bodies from the dead cells contributed to the calcification process by serving as feeding sites.

Figure 6a displays the cell count ratio for each cell type at the beginning and end of the simulation. The figure reveals a decrease in the number of quiescent cells and an emergence of dead cells toward the end of the simulation. Furthermore, it indicates that there were no significant numbers of aVEC, aVIC, and OST at the beginning and the end of the simulation. However, by plotting the cell population data over time, one can monitor the dynamics of different cell types as illustrated in Fig. 7.

Activated cells grow and proliferate through the process of mitosis, depending on the availability of nutrients in their vicinity. Figure 6b illustrates the mitosis of activated cells, wherein new daughter cells are produced during the simulation. The figure highlights that the number of mitotic aVICs is greater than that of aVECs. This disparity is attributed to the higher number of VIC activations compared to VECs, as depicted in Fig. 5.

Activated cells exhibit higher migratory properties, allowing them to reach deeper parts of the tissue and settle in regions with lower TGF $\beta$  concentrations, which can cause them to revert to a quiescent state. This phenomenon explains the observed jump in the qVIC population at 60 to 70 h mark (Fig. 7b) and the corresponding drop in the aVIC population at around the the same time (Fig. 7e). Moreover, activated cells proliferate new daughter cells through mitosis, resulting in sudden increases in the activated cell populations, as depicted in Fig. 7d, e. If these cells survive, they eventually either revert to the quiescent state or differentiate into osteoblast-like cells.

The population of osteoblast-like cells increases as more cells differentiate from activated cells. However, the excessive growth of nodules around them can lead to insufficient access to surrounding nutrients, resulting in cell death and a decrease in the population around 120 h after the start of the simulation (Fig. 7c). The DEAD cell population increases over time as more fiber bundles and nodules appear due to fibrosis and calcification, respectively, as illustrated in Fig. 7f.

## 3.3 Fibrosis

In the simulation, fiber bundles are classified as initial or fibrotic. While initial fiber bundles were randomly distributed throughout the ECM domain at the beginning of the simulation, fibrotic fibers were formed through the process of fibrosis during the simulation. The initial fibers were degraded by MMP-9 secreted from aVICs and aVECs. Figure 8a shows the distribution of initial fiber bundles (iFibers) throughout the tissue depth at different times. It is revealed that degradation of fibers occurred up to a depth of approximately  $100~\mu m$ , and there was no significant fiber degradation after about 90 h. Approximately 23.4% of the iFibers were degraded during the simulation.

The aVICs and aVECs secrete ECM components such as collagen fibers based on the  $\alpha$ SMA concentration in their subcellular models. The distribution of fibrotic fibers is shown in Fig. 8b, which indicates an accumulation of fibers over time. The presence of aVICs and aVECs drove fibrosis



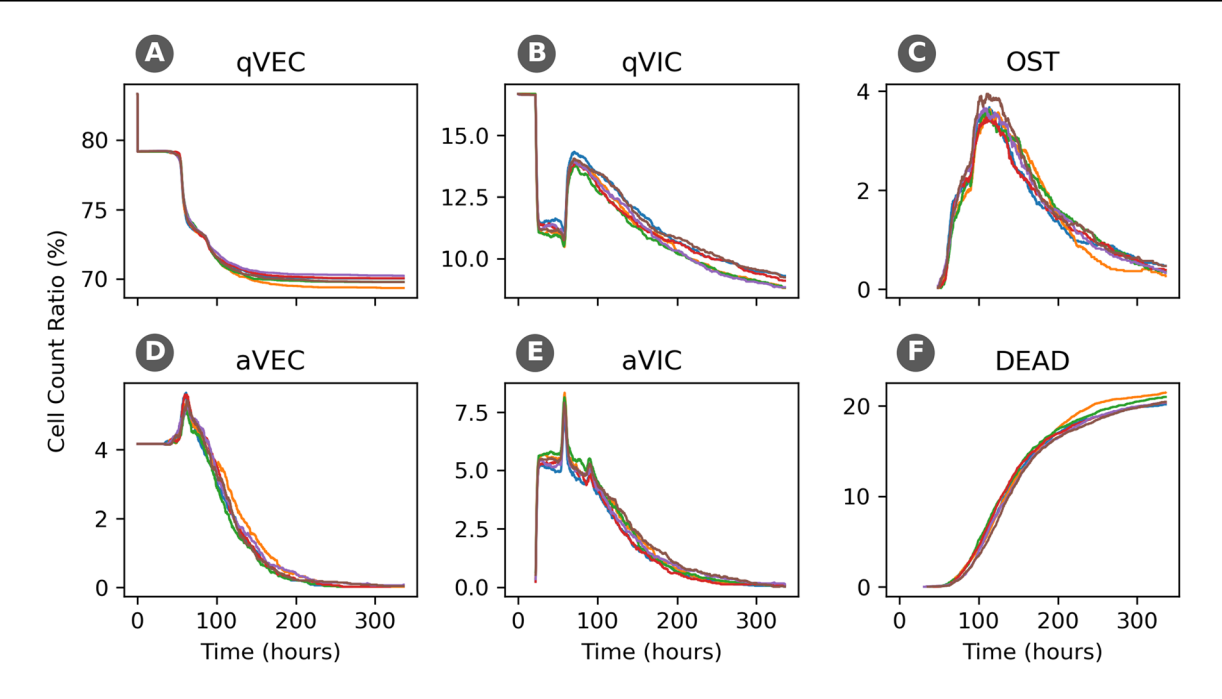
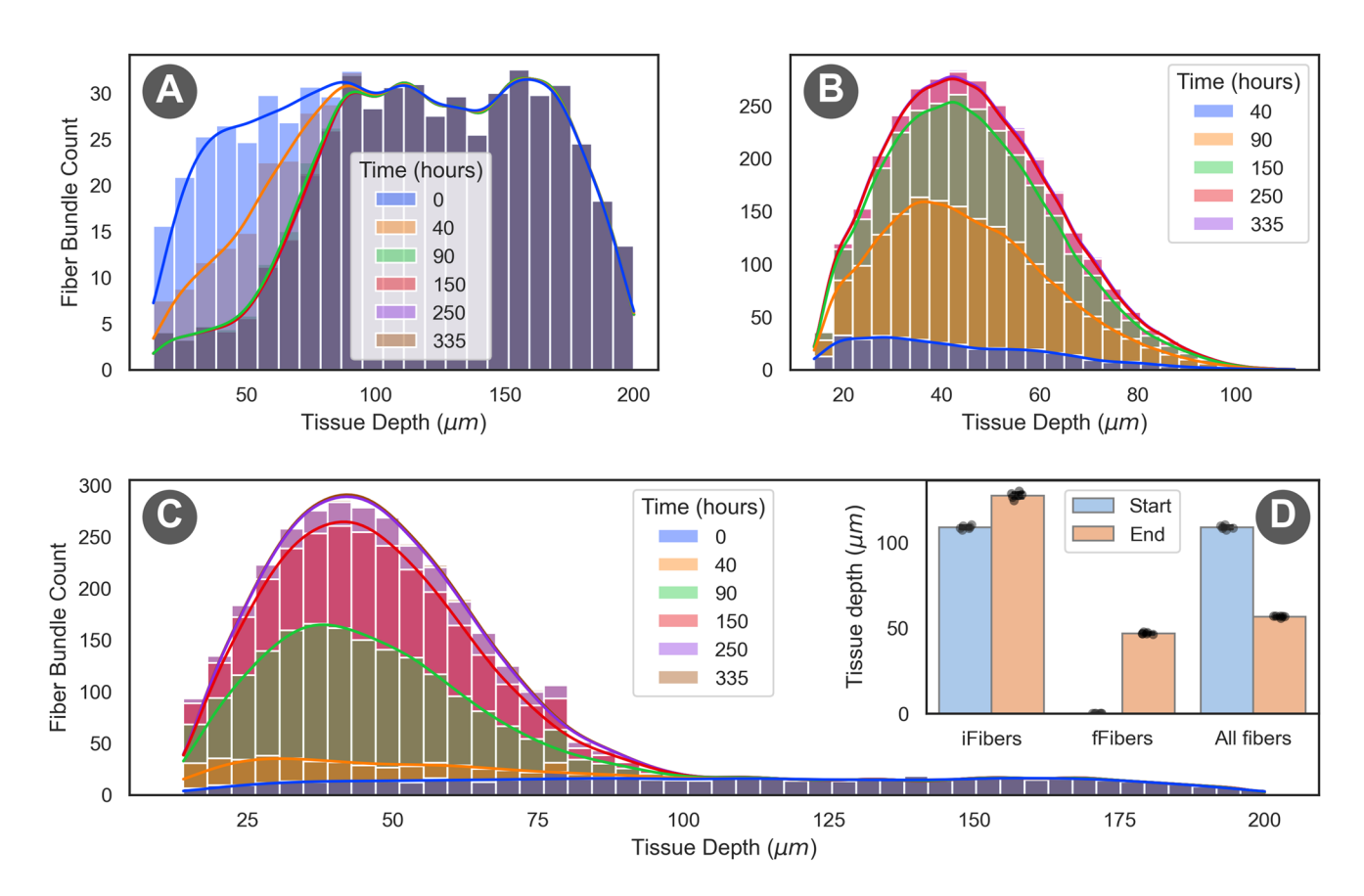


Fig. 7 Cell count ratio of different types during the simulation from six runs with different random seedings. a qVECs, b qVICs, c OSTs, d aVECs, e aVICs, f DEADs. Cell count ratio for a specific cell type

is calculated by dividing the number of each specific cell type by the total number of cells in the model at a given time



**Fig. 8** Fiber bundles statistics from the simulations. **a** distribution of iFibers within the tissue over time; **b** distribution of fFibers generated by the fibrosis activities of aVICs and aVECs over time; **c** distribu-

tion of all fiber bundles (iFibers plus fFibers) over time;  $\mathbf{d}$  comparison of the average fiber bundle depth at the start and the end of the simulations



by secretion of collagen fibers, and the fibrosis activity was high up to around 150 h and became low beyond 250 h. This is consistent with the population of activated cells shown in Fig. 7d, e.

Figure 8c shows the distribution of all fiber bundles in the tissue, including both iFibers and fFibers. The accumulation of fibrotic fibers shifted the overall distribution of all fibers in the tissue, resulting in a peak around 45  $\mu$ m depth. Figure 8d shows the average fiber depths at the start and the end of the simulation. For iFibers, the average depth shifted toward deeper regions as a result of iFiber degradation in the shallower areas. Fibrotic fibers, on the other hand, were mostly generated in the shallower depths. In fact, during the simulation the fibrosis activities deposited about 5.5 times more fiber bundles than the number of iFibers at the start of the simulation. Because of the abundance of generated fFibers in the shallower regions, the average depth of all fibers decreased from about 110 to 60  $\mu$ m.

## 3.4 Calcification

Calcium nodule formation is initiated by the osteoblast-like cells, and apoptotic bodies and cell fragments serve as feeding sites for the nodules to grow. The nodule density in the tissue over time is depicted in Fig. 9a, showing that the first nodules appear after approximately 50 h and increase gradually. This finding is consistent with a previous calcification experiment treated with  $TGF\beta$  (Clark-Greuel et al. 2007). The number of new nodule formation is dependent on the OST population, and as this population decreases, the nodule density does not increase further and reaches a plateau.

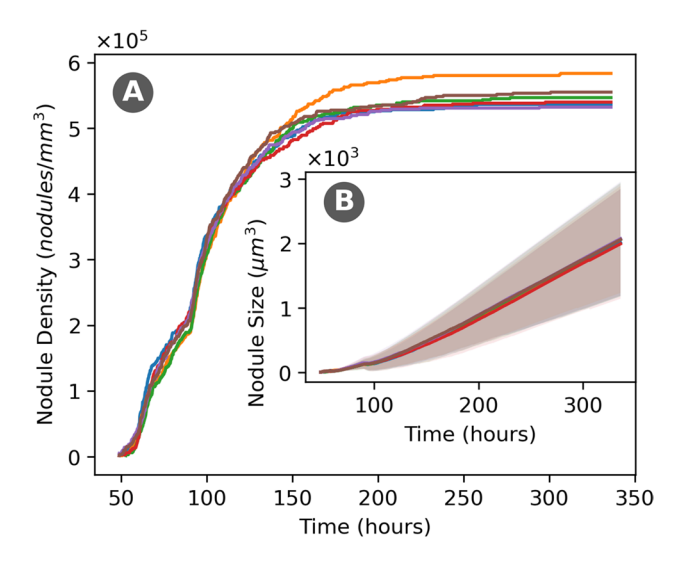


**Fig. 9** Nodule data in six simulation runs with different random seedings. **a** Nodule density, calculated as the total number of nodules per volume of the tissue domain. **b** Nodule size, defined as volume per nodule. The line trace represents the average nodule size while the shaded area represents the nodule size standard deviation

The growth rate of nodule size can vary depending on the location of the nodule and its proximity to apoptotic bodies. These cell fragments release factors that stimulate calcification (Hutcheson et al. 2013), and nodules with more common surface area in contact with apoptotic bodies grow faster than those without cell fragments nearby. This variability in nodule size increased over time, evident in Figs. 9b and 10a. The average nodule size is approximately 2000  $\mu m^3$  at 336 h after the start of the simulation, which is consistent with reported experimental results, showing about 79 percent agreement with our computational findings. (Mendoza et al. 2022).

Figure 10b displays the distribution of nodules across the depth of the tissue at different time points. The graph illustrates that at the early stages of the simulation the nodules initially appeared in shallower regions of the tissue, but as time progressed the distribution shifted toward the deeper regions. The observed trend can be explained by the migratory behavior of activated cells. Due to the presence of the endothelial cell layer acting as a nonpenetrable barrier, the activated cells were biased toward migrating to the deeper parts of the tissue. Once in the deeper regions, the activated cells had the potential to undergo differentiation into osteoblast-like cells, resulting in more nodule formation.

The results from an experimental study by Stephens et al. (2011) show that prenodules tend to form at the shallower parts of aortic tissue, predominantly in the fibrosa section. Our simulation results support these findings, suggesting that this phenomenon primarily stems from the interplay between the diffusion and decay of  $TGF\beta$  in the tissue, where the presence of  $TGF\beta$  at certain depths serves as a trigger for the activation of fibroblasts, ultimately leading to fibrosis and calcification in specific regions.

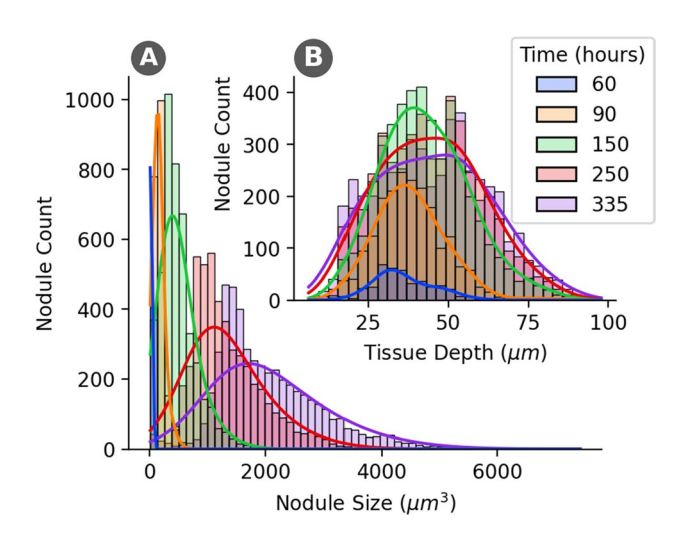


Fig. 10 Time evolution of nodule size distribution. a Nodule size distribution. b Nodule location distribution in terms of depth in tissue



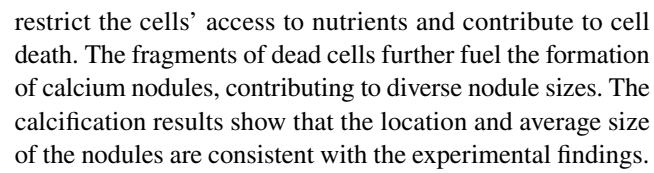
## 3.5 Limitations

To the best of our knowledge, this model for calcification in CAVD using CPM is a pioneering effort. While the current model provides a novel tool for simulating CAVD and other similarly intricate biological processes, there remain limitations. Given that the CPM does not rely on traditional stress-strain formulations, it is not able to capture the mechanical responses of the tissue during remodeling. Consequently, this study does not consider the activation of TGF $\beta$  within the tissue in response to structural stress. Additionally, beyond the TGF $\beta$  signaling pathway, other hypothesized factors that may play a role in initiating and regulating the calcification process in CAVD. BMP, LDL, monocytes, for example, are not addressed in this study. Our model will require further development to incorporate other relevant signaling pathways to better mirror real-life human conditions.

For most of the model's parameters, we sourced them from reported experimental and computational studies. However, in cases where pertinent parameters and their values were readily unavailable in the literature, we either chose them through numerical experimentation to ensure their physiological relevance or employed heuristic reasoning to make estimation. This involved using the averaged result or a qualitative assessment of what appeared to be most appropriate within the context of our study. We plan to continue development of our models by expanding the parameter sets with additional experimentation to better capture the human CAVD process.

## 4 Conclusion

This study describes a multiscale computational model and simulation of calcification in aortic valve tissue, with a focus on the role of TGF $\beta$  stimulation. The model includes a subcellular component of the TGF $\beta$  signaling pathway for each cell, as well as a tissue-scale component that incorporates interactions between cells, ECM proteins, and diffusing cytokines. The model tracks changes in cell population and phenotype, including transitions between different types and states. The ECM is represented as fiber bundles with associated diffusion fields, and fibrosis activity is quantified by measuring the deposition of fiber bundles. Following the differentiation of osteoblast-like cells, calcification occurs through nucleation and growth over time. According to the results, MMP-9 secreted by aVECs and aVICs contributes to the degradation of the initially present fibers while also depositing collagen fibers through fibrosis. Additionally, the occurrence of fibrosis and calcification processes is prevalent at shallower regions of the tissue. The deposition of fibers during fibrosis and the appearance of calcified nodules



The multiscale model presented in this study has the potential to unravel the complexity of CAVD by incorporating various subcellular models and integrating them with a fiber-based tissue-scale model. This methodology enables comprehensive studies of tissue remodeling, not only in CAVD but also in diseases related to cell mechanobiology, such as cancer.

Supplementary Information The online version contains supplementary material available at https://doi.org/10.1007/s10237-023-01793-4.

**Acknowledgements** This work was funded by the National Science Foundation under Grant CMMI 1919438.

**Author Contributions** JA-B, GJM, BTM, and PH contributed to the study conception and outlined the paper. JA-B performed all of the simulations and made figures. JA-B wrote the first draft of the manuscript and GJM, BTM, and PH commented on the previous versions of the manuscript. The final manuscript was read and approved by JA-B, GJM, BTM, and PH.

## **Declarations**

Conflict of interest The authors declare that they have no competing or financial interests.

# References

Abdelhalim MAK (2011) The effects of size and period of administration of gold nanoparticles on rheological parameters of blood plasma of rats over a wide range of shear rates: in vivo. Lipids Health Dis 10:191. https://doi.org/10.1186/1476-511X-10-191

Ahamed J, Burg N, Yoshinaga K, Janczak CA, Rifkin DB, Coller BS (2008) In vitro and in vivo evidence for shear-induced activation of latent transforming growth factor-β1. Blood 112:3650–3660. https://doi.org/10.1182/blood-2008-04-151753

Aikawa E, Libby P (2017) A rock and a hard place: chiseling away at the multiple mechanisms of aortic stenosis. Am Heart Assoc 135(2)

Amindari A, Saltik L, Kirkkopru K, Yacoub M, Yalcin HC (2017)
Assessment of calcified aortic valve leaflet deformations and blood flow dynamics using fluid–structure interaction modeling. Inform Med Unlocked 9:191–199

Anderson ARA (20056) A hybrid mathematical model of solid tumour invasion: the importance of cell adhesion. Math Med Biol A J IMA 22:163–186. Retrieved from http://academic.oup.com/imammb/article/22/2/163/770979/A-hybrid-mathematical-model-of-solid-tumour, https://doi.org/10.1093/imammb/dqi005

Ankeny RF, Thourani VH, Weiss D, Vega JD, Taylor WR, Nerem RM, Jo H (2011) Preferential activation of smad1/5/8 on the fibrosa endothelium in calcified human aortic valves-association with low bmp antagonists and smad6. PLoS ONE 6(6):e20969

Arzani A, Masters KS, Mofrad MR (2017) Multiscale systems biology model of calcific aortic valve disease progression. ACS Biomater Sci Eng 3(11):2922–2933



- Bakhaty AA, Mofrad MR (2015) Coupled simulation of heart valves: applications to clinical practice. Ann Biomed Eng 43:1626–1639
- Balachandran K, Sucosky P, Yoganathan AP (2011) Hemodynamics and mechanobiology of aortic valve inflammation and calcification. Int J Inflamm 2011
- Benjamin EJ, Muntner P, Alonso A, Bittencourt MS, Callaway CW, Carson AP (2019) Heart disease and stroke statistics–2019 update: a report from the American heart association. Circulation 139(10):e56–e528
- Bischoff J (2019) Endothelial-to-mesenchymal transition. Circ Res 124:1163–1165. https://doi.org/10.1161/CIRCRESAHA.119. 314813
- Bosse K, Hans CP, Zhao N, Koenig SN, Huang N, Guggilam A et al (2013) Endothelial nitric oxide signaling regulates Notch1 in aortic valve disease. J Mol Cell Cardiol 60:27–35. https://doi.org/10.1016/j.yjmcc.2013.04.001
- Bustamante DJ, Basile EJ, Hildreth BM, Browning NW, Jensen SA, Moldovan L, Moldovan NI (2021) Biofabrication of spheroids fusion-based tumor models: computational simulation of glucose effects. Biofabrication 13(3):035010
- Butcher JT, Tressel S, Johnson T, Turner D, Sorescu G, Jo H, Nerem RM (2006) Transcriptional profiles of valvular and vascular endothelial cells reveal phenotypic differences: influence of shear stress. Arterioscler Thromb Vasc Biol 26(1):69–77
- Butcher JT, Simmons CA, Warnock JN et al (2008) Mechanobiology of the aortic heart valve. J Heart Valve Dis 17(1):62
- Butcher JT, Mahler GJ, Hockaday LA (2011) Aortic valve disease and treatment: the need for naturally engineered solutions. Adv Drug Deliv Rev 63(4–5):242–268
- Cartlidge TR, Bing R, Kwiecinski J, Guzzetti E, Pawade TA, Doris MK et al (2021) Contrast-enhanced computed tomography assessment of aortic stenosis. Heart 107(23):1905–1911
- Chandra S, Rajamannan NM, Sucosky P (2012) Computational assessment of bicuspid aortic valve wall-shear stress: implications for calcific aortic valve disease. Biomech Model Mechanobiol 11:1085–1096
- Chen N, Glazier JA, Izaguirre JA, Alber MS (2007) A parallel implementation of the Cellular Potts Model for simulation of cell-based morphogenesis. Comput Phys Commun 176(11–12):670–681
- Chowkwale MS (2019) In silico multiscale modeling of endothelial cell mechanobiology in a tumor microenvironment
- Chowkwale M, Mahler GJ, Huang P, Murray BT (2019) A multiscale in silico model of endothelial to mesenchymal transformation in a tumor microenvironment. J Theor Biol 480:229–240. https://doi.org/10.1016/j.jtbi.2019.08.012
- Chowkwale M, Lindsey ML, Saucerman JJ (2022) Intercellular model predicts mechanisms of inflammation fibrosis coupling after myocardial infarction. J Physiol. https://doi.org/10.1113/JP283346
- Clark-Greuel JN, Connolly JM, Sorichillo E, Narula NR, Rapoport HS, Mohler ER III, Levy RJ (2007) Transforming growth factor-β1 mechanisms in aortic valve calcification: increased alkaline phosphatase and related events. Ann Thorac Surg 83(3):946–953
- Collier IE, Legant W, Marmer B, Lubman O, Saffarian S, Wakatsuki T, Goldberg GI (2011) Diffusion of mmps on the surface of collagen fibrils: the mobile cell surface-collagen substratum interface. PLoS ONE. https://doi.org/10.1371/journal.pone.0024029
- Dayawansa NH, Baratchi S, Peter K (2022) Uncoupling the vicious cycle of mechanical stress and inflammation in calcific aortic valve disease. Front Cardiovasc Med 9:783543
- Dongre A, Weinberg RA (2019) New insights into the mechanisms of epithelial-mesenchymal transition and implications for cancer. Nat Rev Mol Cell Biol 20:69–84. https://doi.org/10.1038/s41580-018-0080-4
- Driscoll K, Cruz AD, Butcher JT (2021) Inflammatory and biomechanical drivers of endothelial-interstitial interactions in calcific aortic valve disease. Circ Res 128(9):1344–1370

- Dutta P, Lincoln J (2018) Calcific aortic valve disease: a developmental biology perspective. Curr Cardiol Rep 20:1–13
- Fortuna I, Perrone GC, Krug MS, Susin E, Belmonte JM, Thomas GL, de Almeida RM (2020) Compucell3d simulations reproduce mesenchymal cell migration on flat substrates. Biophys J 118(11):2801–2815
- Franssen LC, Lorenzi T, Burgess AEF, Chaplain MAJ (2019) A mathematical framework for modelling the metastatic spread of cancer. Bull Math Biol 81:1965–2010. https://doi.org/10.1007/s11538-019-00597-x
- Garg V, Muth AN, Ransom JF, Schluterman MK, Barnes R, King IN, Srivastava D (2005) Mutations in notch1 cause aortic valve disease. Nature 437(7056):270–274
- Gaur T, Lengner CJ, Hovhannisyan H, Bhat RA, Bodine PV, Komm BS et al (2005) Canonical wnt signaling promotes osteogenesis by directly stimulating runx2 gene expression. J Biol Chem 280(39):33132–33140
- Gottesman S (2014) Coordinating bacterial cell division with nutrient availability: a role for glycolysis. mBio. https://doi.org/10.1128/mBio.00935-14
- Graner F, Glazier JA (1992) Simulation of biological cell sorting using a two-dimensional extended potts model. Phys Rev Lett 69(13):2013
- Heino J (2007) The collagen family members as cell adhesion proteins. BioEssays 29(10):1001–1010
- Hjortnaes J, Shapero K, Goettsch C, Hutcheson JD, Keegan J, Kluin J, Aikawa E (2015) Valvular interstitial cells suppress calcification of valvular endothelial cells. Atherosclerosis 242:251–260. https:// doi.org/10.1016/j.atherosclerosis.2015.07.008
- Horn MA, Trafford AW (2016) Aging and the cardiac collagen matrix: Novel mediators of fibrotic remodelling. J Mol Cell Cardiol 93:175–185. https://doi.org/10.1016/j.yjmcc.2015.11.005
- Hutcheson JD, Chen J, Sewell-Loftin M, Ryzhova LM, Fisher CI, Su YR, Merryman WD (2013) Cadherin-11 regulates cell-cell tension necessary for calcific nodule formation by valvular myofibroblasts. Arterioscler Thromb Vasc Biol 33(1):114–120
- Jafari Nivlouei S, Soltani M, Shirani E, Salimpour MR, Travasso R, Carvalho J (2022) A multiscale cell-based model of tumor growth for chemotherapy assessment and tumor-targeted therapy through a 3d computational approach. Cell Prolif 55(3):e13187
- Jian B, Narula N, Li Q-Y, Mohler ER III, Levy RJ (2003) Progression of aortic valve stenosis: Tgf-β1 is present in calcified aortic valve cusps and promotes aortic valve interstitial cell calcification via apoptosis. Ann Thorac Surg 75(2):457–465
- Kabla AJ (2012) Collective cell migration: leadership, invasion and segregation. J R Soc Interface 9(77):3268–3278
- Kawamoto M, Matsunami T, Ertl RF, Fukuda Y, Ogawa M, Spurzem JR, Rennard SI (1997) Selective migration of α-smooth muscle actin-positive myofibroblasts toward fibronectin in the Boyden's blindwell chamber. Clin Sci 93(4):355–362
- Keller EF, Segel LA (1971) Model for chemotaxis. J Theor Biol 30(2):225–234
- Nekolla K, Rehberg M, Vollmar AM, Zahler S (2016) New view on endothelial cell migration. Arterioscler Thromb Vasc Biol 36:2346–2357. https://doi.org/10.1161/ATVBAHA.116.307870
- Kick K, Nekolla K, Rehberg M, Vollmar AM, Zahler S (2016) New view on endothelial cell migration: switching modes of migration based on matrix composition. Arterioscler Thromb Vasc Biol 36(12):2346–2357
- Kumar S, Kapoor A, Desai S, Inamdar MM, Sen S (2016) Proteolytic and non-proteolytic regulation of collective cell invasion: tuning by ECM density and organization. Sci Rep 6:19905. https://doi. org/10.1038/srep19905
- Kumarswamy R, Volkmann I, Jazbutyte V, Dangwal S, Park D-H, Thum T (2012) Transforming growth factor-β-induced endothelialto-mesenchymal transition is partly mediated by



- MicroRNA-21. Arterioscler Thromb Vasc Biol 32:361–369. https://doi.org/10.1161/ATVBAHA.111.234286
- Lee B, Zhou X, Riching K, Eliceiri KW, Keely PJ, Guelcher SA, Jiang Y (2014) A three-dimensional computational model of collagen network mechanics. PLoS ONE 9:e111896. https://doi.org/10.1371/journal.pone.0111896
- Leopold JA (2012) Cellular mechanisms of aortic valve calcification. Circ Cardiovasc Interv 5(4):605–614
- Luraghi G, Migliavacca F, Chiastra C, Rossi A, Reimers B, Stefanini GG, Matas JFR (2019) Does clinical data quality affect fluid-structure interaction simulations of patient-specific stenotic aortic valve models? J Biomech 94:202–210
- Ma X, Zhao D, Yuan P, Li J, Yun Y, Cui Y et al (2020) Endothelialto-mesenchymal transition in calcific aortic valve disease. Acta Cardiol Sin 36(3):183
- Mahler GJ, Farrar EJ, Butcher JT (2013) Inflammatory cytokines promote mesenchymal transformation in embryonic and adult valve endothelial cells. Arterioscler Thromb Vasc Biol 33:121–130. https://doi.org/10.1161/ATVBAHA.112.300504
- Maleki H, Shahriari S, Durand LG, Labrosse MR, Kadem L (2014) A metric for the stiffness of calcified aortic valves using a combined computational and experimental approach. Medical Biol Eng Comput 52:1–8
- Masjedi S, Lei Y, Patel J, Ferdous Z (2017) Sex-related differences in matrix remodeling and early osteogenic markers in aortic valvular interstitial cells. Heart Vessels 32(2):217–228. https:// doi.org/10.1007/s00380-016-0909-8
- Masur SK, Dewal HS, Dinh TT, Erenburg I, Petridou S (1996) Myofibroblasts differentiate from fibroblasts when plated at low density. Proc Natl Acad Sci 93:4219–4223. https://doi.org/10. 1073/pnas.93.9.4219
- Mathieu P, Bouchareb R, Boulanger M-C (2015) Innate and adaptive immunity in calcific aortic valve disease. J Immunol Res 2015
- Mendoza M, Chen M-H, Huang P, Mahler GJ (2022) Shear and endothelial induced late-stage calcific aortic valve disease-on-achip develops calcium phosphate mineralizations. Lab Chip 22:1374–1385. https://doi.org/10.1039/D1LC00931A
- ming Meng X, Nikolic-Paterson DJ, Lan HY (2016) TGF-β: the master regulator of fibrosis. Nat Rev Nephrol 12:325–338. https://doi.org/10.1038/nrneph.2016.48
- Mirza A, Ramaswamy S (2022) Importance of non-newtonian computational fluid modeling on severely calcified aortic valve geometries-insights from quasi-steady state simulations. J Biomech Eng 144(11):114501
- Misfeld M, Sievers H-H (2007) Heart valve macro-and microstructure. Philos Trans Roy Soc B Biol Sci 362(1484):1421–1436
- Nguyen Edalgo YT, Zornes AL, Ford Versypt AN (2019) A hybrid discrete-continuous model of metastatic cancer cell migration through a remodeling extracellular matrix. AIChE J 65(9):e16671
- Nkomo VT, Gardin JM, Skelton TN, Gottdiener JS, Scott CG, Enriquez-Sarano M (2006) Burden of valvular heart diseases: a population-based study. The Lancet 368(9540):1005–1011
- O'Brien F, Harley B, Yannas I, Gibson L (2005) The effect of pore size on cell adhesion in collagengag scaffolds. Biomaterials 26:433–441. https://doi.org/10.1016/j.biomaterials.2004.02.052
- O'Brien J, Lyons T, Monks J, Lucia MS, Wilson RS, Hines L, Schedin P (2010) Alternatively activated macrophages and collagen remodeling characterize the postpartum involuting mammary gland across species. Am J Pathol 176(3):1241–1255
- Osman L, Yacoub MH, Latif N, Amrani M, Chester AH (2006) Role of human valve interstitial cells in valve calcification and their response to atorvastatin. Circulation 114:547–552. https://doi.org/ 10.1161/CIRCULATIONAHA.105.001115
- Phan SH (2008) Biology of fibroblasts and myofibroblasts. Proc Am Thorac Soc 5(3):334–337

- Pho M, Lee W, Watt DR, Laschinger C, Simmons CA, McCulloch CA (2008) Cofilin is a marker of myofibroblast differentiation in cells from porcine aortic cardiac valves. Am J Physiol Heart Circ Physiol 294:H1767–H1778. https://doi.org/10.1152/ajpheart. 01305.2007
- Piek A, de Boer RA, Silljé HHW (2016) The fibrosis-cell death axis in heart failure. Heart Fail Rev 21:199–211. https://doi.org/10.1007/s10741-016-9536-9
- Rajamannan NM, Evans FJ, Aikawa E, Grande-Allen KJ, Demer LL, Heistad DD et al (2011) Calcific aortic valve disease: not simply a degenerative process a review and agenda for research from the national heart and lung and blood institute aortic stenosis working group. Circulation 124(16):1783
- Ramis-Conde I, Drasdo D, Anderson AR, Chaplain MA (2008) Modeling the influence of the E-cadherin-β-catenin pathway in cancer cell invasion: a multiscale approach. Biophys J 95(1):155–165
- Rush MN (2018) Chemically modified monolayer surfaces influence valvular interstitial cell attachment and differentiation for heart valve tissue engineering (Unpublished doctoral dissertation)
- Sadrabadi MS, Eskandari M, Feigenbaum HP, Arzani A (2021a) Local and global growth and remodeling in calcific aortic valve disease and aging. J Biomech 128:110773
- Sadrabadi MS, Hedayat M, Borazjani I, Arzani A (2021b) Fluidstructure coupled biotransport processes in aortic valve disease. J Biomech 117:110239
- Sarper M, Cortes E, Lieberthal TJ, del Río Hernández A (2016) Atra modulates mechanical activation of tgf-β by pancreatic stellate cells. Sci Rep 6(1):27639
- Sánchez-Duffhues G, de Vinuesa AG, ten Dijke P (2018) Endothelial-to-mesenchymal transition in cardiovascular diseases: developmental signaling pathways gone awry. Dev Dyn 247:492–508. https://doi.org/10.1002/dvdy.24589
- Son KJ, Gheibi P, Stybayeva G, Rahimian A, Revzin A (2017) Detecting cell-secreted growth factors in microfluidic devices using bead-based biosensors. Microsyst Nanoeng 3(1):17025. https://doi.org/10.1038/micronano.2017.25
- Steitz SA, Speer MY, McKee MD, Liaw L, Almeida M, Yang H, Giachelli CM (2002) Osteopontin inhibits mineral deposition and promotes regression of ectopic calcification. Am J Pathol 161(6):2035–2046. https://doi.org/10.1016/S0002-9440(10) 64482-3
- Stephens EH, Saltarrelli JG, Baggett LS, Nandi I, Kuo JJ, Davis AR, Grande-Allen KJ (2011) Differential proteoglycan and hyaluronan distribution in calcified aortic valves. Cardiovasc Pathol 20(6):334–342
- Sucosky P, Balachandran K, Elhammali A, Jo H, Yoganathan AP (2009) Altered shear stress stimulates upregulation of endothelial vcam-1 and icam-1 in a bmp-4-and tgf-β1-dependent pathway. Arterioscler Thromb Vasc Biol 29(2):254–260
- Swat MH, Thomas GL, Belmonte JM, Shirinifard A, Hmeljak D, Glazier JA (2012) Multi-scale modeling of tissues using compucell3d. In: Methods in cell biology, vol 110. Elsevier, pp 325–366
- Taylor PM (2007) Biological matrices and bionanotechnology. Philos Trans Roy Soc B Biol Sci 362(1484):1313–1320
- Thampatty BP, Wang JH-C (2007) A new approach to study fibroblast migration. Cell Motil Cytoskelet 64(1):1–5
- Wakefield LM, Winokur TS, Hollands RS, Christopherson K, Levinson AD, Sporn MB (1990) Recombinant latent transforming growth factor beta 1 has a longer plasma half-life in rats than active transforming growth factor beta 1, and a different tissue distribution. J Clin Investig 86:1976–1984. https://doi.org/10.1172/JCI114932
- Weinberg EJ, Kaazempur Mofrad MR (2007) Transient, three-dimensional, multiscale simulations of the human aortic valve. Cardiovasc Eng 7:140–155
- Welsh C, Xu J, Smith L, König M, Choi K, Sauro HM (2023) libRoad-Runner 2.0: a high performance SBML simulation and analysis



library. Bioinformatics. https://doi.org/10.1093/bioinformatics/btac770

Yutzey KE, Demer LL, Body SC, Huggins GS, Towler DA, Giachelli CM et al (2014) Calcific aortic valve disease: a consensus summary from the alliance of investigators on calcific aortic valve disease. Arterioscler Thromb Vasc Biol 34(11):2387–2393

**Publisher's Note** Springer Nature remains neutral with regard to jurisdictional claims in published maps and institutional affiliations.

Springer Nature or its licensor (e.g. a society or other partner) holds exclusive rights to this article under a publishing agreement with the author(s) or other rightsholder(s); author self-archiving of the accepted manuscript version of this article is solely governed by the terms of such publishing agreement and applicable law.

